Electrochimica Acta 318 (2019) 865–874

Contents lists available at ScienceDirect

Electrochimica Acta

journal homepage: www.elsevier.com/locate/electacta

Free-standing macro-porous nitrogen doped graphene film for high energy density supercapacitor

Yanan Jin [a, b], Yuena Meng [a, *], Wei Fan [b, **], Hengyi Lu [b], Tianxi Liu [b], Sixin Wu [a]

[a] Key Laboratory for Special Functional Materials of Ministry of Education, National & Local Joint Engineering Research Centre for High-efficiency Display and Lighting Technology, School of Materials and Engineering, Collaborative Innovation Centre of Nano Functional Materials and Applications, Henan University, Kaifeng, China

[b] State Key Laboratory for Modification of Chemical Fibers and Polymer Materials, College of Materials Science and Engineering, Donghua University, 2999 North Renmin Road, Shanghai 201620, PR China

ARTICLE INFO

Article history:
Received 11 April 2019
Received in revised form
12 June 2019
Accepted 17 June 2019
Available online 19 June 2019

Keywords:
Graphene aerogel film
Supercapacitors
N-doped carbon material
Free-standing

ABSTRACT

In this paper, a porous free-standing nitrogen-doped graphene (NG) film for high energy density supercapacitor is prepared via a facile hydrogel strategy. Taking advantage of the hydrogel behavior together with the mechanical stability of GO sheets, an interconnected macro-porous nitrogen-doped free-standing film is constructed. The nitrogen doping structure ensures sufficient pseudocapacitance and conductivity of the film, while the macro-porous structure favors fast ion adsorption. When assembled in a symmetric two-electrode supercapacitor, not any conductive agent or binder is used. The free-standing NG film shows specific capacitance of 455.4 F g^{-1} based on the mass of whole electrode, while no capacitance loss after 5000 cycles. Furthermore, an asymmetric supercapacitor is assembled with this NG film as negative electrode and a macro-porous graphene/polypyrrole composite film synthesized using the similar strategy as positive electrode. An energy density of 34.51 Wh kg^{-1} at a power density of 849.77 W kg^{-1} is obtained, suggesting great potential of this film for application in energy storage field.

1. Introduction

Among diverse energy storage systems, supercapacitors (SCs) draw considerable attention due to their higher power density, longer cycle life, simpler fabricating procedure and safety compared with lithium-ion batteries [1–6]. Among the functional parts of a typical SC device, including electrode, separator and electrolyte [7], the electrode materials are the key to determine electrochemical performance of the device [8]. According to the energy storage mechanism [6], SCs can be classified into electric double-layer capacitors (EDLCs) and pseudo-capacitors. Carbon materials, as typical EDLC materials, are the most common electrode materials, possessing high power density and long cycle life. However their energy storage ability is largely limited by their physical charge storage mechanism. Oppositely, pseudo-capacitor materials can achieve higher energy density than EDLCs due to fast redox reactions, but at the cost of loss in rate capability and cyclability [9–12]. To combine the advantages of both, nitrogen doped carbon materials, cooperating nitrogen atoms into carbon lattice, have been widely studied [13–15]. Huang et al. [16] synthesized N-doped mesoporous few-layer carbon by combining chemical vapor deposition and template method, which provides a specific capacitance of 855 F g^{-1} and exhibits good cycling stability. Hu et al. [17] obtained unique 3D hierarchical nitrogen-doped carbon nanocages, achieving a high energy density of 10.90 Wh kg^{-1} at 22.22 kW kg^{-1}, as well as superior rate capability and cycling stability. More recently, Deng et al. [18] prepared nitrogen-doped carbon material with a specific area of 2905.4 m^2 g^{-1} and a specific capacitance of 350.7 F g^{-1} (at a current density of 1 A g^{-1}) in 1 M H_2SO_4 electrolyte. The above researches demonstrate that nitrogen-doped carbon materials with interconnected porous structure and large specific surface area exhibit high specific capacitance and good stability. This mainly attributes to abundant redox active sites provided by the porous nitrogen doping structure and efficient pathways for ion diffusion and electron transmission [19–21].

* Corresponding author.
** Corresponding author.
E-mail addresses: mengyuena@henu.edu.cn (Y. Meng), weifan@dhu.edu.cn (W. Fan).

https://doi.org/10.1016/j.electacta.2019.06.107
0013-4686/

However, just like most active materials, conventional powder porous nitrogen-doped carbon materials must work with the aid of conductive agents and binders [22] for electrochemical application, which will definitely decrease the performance of the whole electrode. Integrate film electrodes, which can stand steady without the aid of any additives, are highly competitive for practical use. On the one hand, using of them eliminates the mass of inactive part of the electrode, improving the energy density of the whole electrode. On the other hand, the surface of the active material of free-standing electrode is not stuck by the additives, which can achieve abundant energy storage sites and further high electrochemical properties [23–26]. Moreover, the mechanical integrity shows potential in flexible devices. There are few reports about NC based integrated electrodes. Choi et al. [27] developed nitrogen-doped graphene supported on nickel and paper substrates by a plasma-enhanced chemical vapor deposition process. The capacitance reaches 280 F g^{-1}, which is about 4 times larger than the undoped graphene electrode. After 10000 cycles, the flexible supercapacitor displayed 95.3% of its initial capacitance, showing excellent cycling stability. Yu et al. [28] prepared flexible nitrogen-doped activated nanofiber network which showed ~95.9% retention of its initial capacitance after 5000 cycles. Wong et al. [29] prepared free-standing nitrogen-doped hierarchically porous carbon foam via annealing of soft-template-casted melamine foam. The capacitance of the symmetric supercapacitor delivered a high capacitance of 59.4 F g^{-1} at 0.5 A g^{-1}. After 10000 cycles, the supercapacitor performed excellent capacitance retention of 91.5%. Liu et al. [30] synthesized 3D porous nitrogen-doped graphene-CNT hybrid paper through using polystyrene colloidal particles as template followed by carbonization. There was only less than 3% capacitance loss after 1000 charge/discharge cycles, revealing a good cycling stability.

Although the reported free-standing nitrogen doped carbon electrodes already show good cyclability. The energy density still needs to be improved to accommodate further applications. Several aspects can affect the specific energy density, including the density and the mass loading of the electrode [31], the morphology and conductivity of electrodes [32], and the type of the electrolyte used [33] and so on. A critical factor to enhance energy density without sacrificing rate performance and other essential properties is to achieve rich and fully exposed energy storage sites in the electrode. That means to ensure fast ion transport and facilitate redox kinetics. Hence, interconnected porous structure with enhanced surface area is desirable. However, it is still a challenge to achieve such structure in a freestanding nitrogen doped carbon electrode. A main reason is that porous NC electrodes are usually fabricated by chemical activation or template method, which is rather complicated and not suitable to maintain an integrate structure.

In this study, we fabricated a free-standing N-doped graphene aerogel (NG) film via vacuum filtration, direct freeze drying and pyrolysis. The result flexible film incorporates two well-connected parts, the upper NG aerogel and the lower porous reduced graphene oxide (RGO) sheets section. This film shows a three dimensional macro-porous structure from top to bottom. On the one hand, the pyridinic and pyrrolic N moieties converted from pyrrole molecule contribute the main redox reactions for energy storage. On the other hand, the adsorption and transport of ions is optimized in the macro-porous structure by adapting the cross linking degree. The two aspects are all conducive to improving the energy density of the film. When assembled in symmetrical two electrode supercapacitor, the specific capacitance of NG film reaches 455.4 F g^{-1}. After 5000 cycles, the capacitance shows no obvious loss. Also, the reduced graphene oxide/polypyrrole (RGO/PPy) aerogel film with the same interconnected macro-porous structure is prepared by a similar procedure but experienced in-situ polymerization process. To further explore the practical performance, an asymmetric supercapacitor was assembled with RGO/PPy composite film as positive electrode material and the NG film as negative electrode material, which achieves a broad operating voltage of 0–1.7 V in aqueous solution, delivering an energy density of 34.51 Wh kg^{-1} at a power density of 849.77 W kg^{-1}. The results demonstrate that this freestanding NG film based electronic device has good application aspect in high-performance energy storage devices.

2. Experimental

2.1. Materials

Natural graphite powder (325 meshes) was purchased from Sigma-Aldrich. Ammonium persulfate (APS), ethanol, 98% H_2SO_4, 30% H_2O_2, potassium permanganate ($KMnO_4$), $NaNO_3$, HI (≥45%), HAc (99.5%) and 37% HCl were supplied by Sinopham Chemical Reagent Co., Ltd. Pyrrole was purchased from Sigma-Aldrich, and distilled before use. All the other chemicals were of analytical grade and used as received without further purification. Deionized (DI) water was used throughout the experiments.

2.2. Preparation of graphite oxide (GO) solution and nitrogen-doped graphene (NG) films

GO was synthesized from natural graphite powder via Hummers' method [34] and dispersed in DI water with ultrasonication to form 0.5 mg mL^{-1} and 6 mg mL^{-1} GO dispersion. A small amount of fresh pyrrole (Py) monomer was mixed with 5 mL 6 mg mL^{-1} GO suspension, with GO/Py weight ratios of 1:1, 1:2, 1:3 and 1:4. The mixture was shaken violently for a few seconds and sonicated for another 15 min. After keeping still for 6 h, the mixture was filtrated after filtration of 20 mL 0.5 mg mL^{-1} GO suspension through a Poly (tetra fluoroethylene) (PTFE) filter membrane (220 nm pore size). To obtain free-standing film, the filtered substance was freeze-dried together with the membrane and then carefully peeled off. Finally, the freeze-dried film was carbonized under pure nitrogen gas atmosphere at 600 °C for 2 h with a heating rate of 5 °C min^{-1}. Therefore, several graphene films with various amounts of doped nitrogen were obtained, which were named as NG-1, NG-2, NG-3 and NG-4 according to different ratio of Py: GO, respectively. The volume of the mixture used for filtration was constant. For comparison, RGO film was fabricated using the same amount of GO in a similar way but with no Py monomer, which was named as NG-0.

2.3. Fabrication of RGO/PPy composite films

RGO/PPy composite films were synthesized by solution polymerization of Py on the as above freeze-dried GO film with the GO/pyrrole weight ratio of 1:3. Typically, a piece of freeze-dried GO film got according to above processes was placed in 20 mL of 1 M HCl aqueous solution in an ice bath. Successively, different amounts of Py monomer (the final solution concentration is 0.01 mol L^{-1}, 0.05 mol L^{-1} and 0.1 mol L^{-1}) was added into the solution under stirring to form a uniform mixture, respectively. An aqueous solution of APS was resolved in another 10 mL HCl aqueous solution and precooled (the molar ratio of APS to Py is 1:1). The polymerization was started when the oxidant solution was added to the monomer solution. After stirring for 24 h in an ice bath, the composited film was taken out from the polymerization system and washed with DI water and ethanol repeatedly. The obtained dark black films was immersed in a mixed HI and HAc solution (the volume ratio is 1:2) at room temperature for 30 min, and then kept at 75 °C for 6 h. Finally, the composite films were washed with water and ethanol several times to ensure iodine and HI was removed completely. The

film was obtained after drying under vacuum at 40 °C for 12 h, named as RGO/PPy-0.01, RGO/PPy-0.05 and RGO/PPy-0.1, according to different amount of Py monomer, respectively. Still, RGO/PPy-0 film was synthesized without adding additional amount of Py monomer in the polymerization for comparison.

2.4. Characterization

The morphology of the samples was investigated by field-emission scanning electron microscopy (FESEM, Ultra 55). X-ray diffraction (XRD) patterns were conducted on an X'Pert Pro X-ray diffractometer equipped with Cu K_α radiation ($\lambda = 0.1542$ nm) under a voltage of 40 kV and a current of 40 mA. Raman spectra were collected using a LabRAM-HR Confocal Laser Micro Raman Spectrometer at an exciting wavelength of 532 nm. Fourier-transform infrared (FTIR) spectra were recorded with a 4 cm^{-1} spectral resolution on a Nicolet Nexus 470 spectrometer equipped with a DTGS detector. X-ray photoelectron spectroscopy (XPS) analyses were accomplished with a VG ESCALAB 220I-XL device. Thermogravimetric analysis (TGA, Pyric 1 TGA, PerkinElmer) were performed in Nitrogen atmosphere from 100 °C to 600 °C at a heating rate of 20 °C min^{-1}.

2.5. Electrochemical measurements

All electrochemical performances were measured on a CHI 660D electrochemical workstation, using a two-electrode system, with a filter paper (Titan 102, cellulose fiber) used as separator and graphite paper (thickness: 0.2 mm) as the current collector. The NG-x films (x = 0, 1, 2, 3 and 4) and RGO/PPy-y composite films (y = 0, 0.01, 0.05 and 0.1) were cut into 10 × 10 mm^2 squares and used directly as binder-free working electrode materials. The detailed thickness and density information of the films are shown in Table S3. Cyclic voltammetry (CV) curves were collected at various scan rates with potential ranges of −1 to 0 V for NG-x (x = 0, 1, 2, 3, 4) films and 0–1 V for RGO/PPy-y (y = 0, 0.01, 0.05 and 0.1) composite films, respectively. Galvanostatic charge-discharge (GCD) curves of the two films under different current densities were measured in the same potential window as their CV test respectively. The electrochemical impedance spectroscopy (EIS) was recorded in the frequency ranging from 0.01 to 10 kHz with amplitude of 5 mV. The specific capacitance (F g^{-1}) of a single electrode was calculated from galvanostatic discharge curves according to the following equation:

$$C = \frac{2It}{mV} \tag{1}$$

where I is the discharge current densities (A), t is the discharge time (s), m is the mass of the whole electrode (g), and V is the potential window (V).

The asymmetric supercapacitor (ASC) was fabricated using RGO/PPy-0.05 film as the positive electrode material and NG-3 film as the negative electrode material. The mass ratio of RGO/PPy-0.05 composite film to NG-3 film was controlled as 0.62 according to the following equations:

$$Q_+ = Q_- \tag{2}$$

$$Q = C \times V \times m \tag{3}$$

$$\frac{m_+}{m_-} = \frac{C_- \times V_-}{C_+ \times V_+} \tag{4}$$

where Q is the stored charge on the cathode or anode (C), C is the specific capacitance (F g^{-1}), V is the potential window (V), m is the mass of the electrode (g).

The gravimetric energy density (E, $Wh\ Kg^{-1}$) and power density (P, $W\ Kg^{-1}$) of the asymmetric supercapacitor were evaluated using equations (5) and (6), respectively:

$$E = \frac{\frac{1}{2}CV^2}{3.6} \tag{5}$$

$$P = \frac{3600E}{t} \tag{6}$$

where C is the specific capacitance of the two-electrode devices (F g^{-1}), V is the potential window (V), and t is the discharge time (s).

3. Results and discussion

3.1. Morphology and chemical characterization of NG-x films (x = 0, 1, 2, 3 and 4) and RGO/PPy-y (y = 0, 0.01, 0.05 and 0.1) composite films

Gel method is a useful route to get macro-porous network structure, especially for graphene bulk materials. However, it is not easy to get film material through hydrogel process because of the loose macro-porous structure. We designed a two-layer structure to reinforce the free-standing stability of the as obtained aerogel structure and enhance the available surface of the free-standing film at the same time. The main synthetic process of NG-x (x = 0, 1, 2, 3, 4) films and RGO/PPy-y (y = 0, 0.01, 0.05 and 0.1) composite films is schematically illustrated in Fig. 1I. To start with, the hybrid hydrogels were prepared by mixing a certain volume of GO suspension with various amounts of Py monomer. Followed by mixing violently, the dark material was observed at the bottom of an inverted centrifuge tube (Fig. 1I), illustrating hydrogel was formed successfully. Subsequently, the hydrogel was filtrated after a certain amount of GO solution to make a uniform film. After freeze-drying and pyrolysis, the final product NG-x film was obtained.

Morphology of NG-x (x = 1, 2, 3, 4) films is shown in Fig. 1(II) and Fig. S1. From SEM images, an porous structure can be clearly observed in NG-2 and NG-3 samples (Fig. 1(II), Fig. S1). This is due to the hydrogel behavior of GO in the presence of Py, where two-dimensional graphene sheets interconnect with each other forming 3D framework structure with enlarged interlayer space. Thus, to a large extent, it prevents graphene sheets from restacking. However, as for NG-1 and NG-4, the macro-pores become not as clear (Fig. S1d). This is because that the amount of Py monomer influences the assemble behavior of GO sheets. The cross-link function between two graphene sheets generally strengthens along with the increasing amount of Py monomer. When there is no sufficient or too much Py monomer, graphene sheets stack with each other severely without forming interconnected pores. As can be seen in the cross-section morphology of NG-3 film (Fig. 1(II) b-d), the upper aerogel show a macro-porous morphology with interconnected 3D framework network. Graphene sheets were arranged in horizontal direction forming aligned macropores in the bottom of NG-3 film. The oriented porous structure endows the film superb mechanical capacity along the film direction as demonstrated previously [35]. It can be concluded that the trend of orientated alignment in horizontal direction favors the upper aerogel linking up with graphene sheets beneath it (Fig. 1(II) c), forming an integrated film. As a result, the NG-3 film shows good flexibility (Figs. S2–3) with thickness of about 400 μm (Fig. 1(II) a). The density of NG-x (x = 1, 2, 3, 4) films is 0.55, 0.45, 0.47 and 0.52 mg cm^{-2}, respectively.

In addition, RGO/PPy-0.05 composite film shows a similar

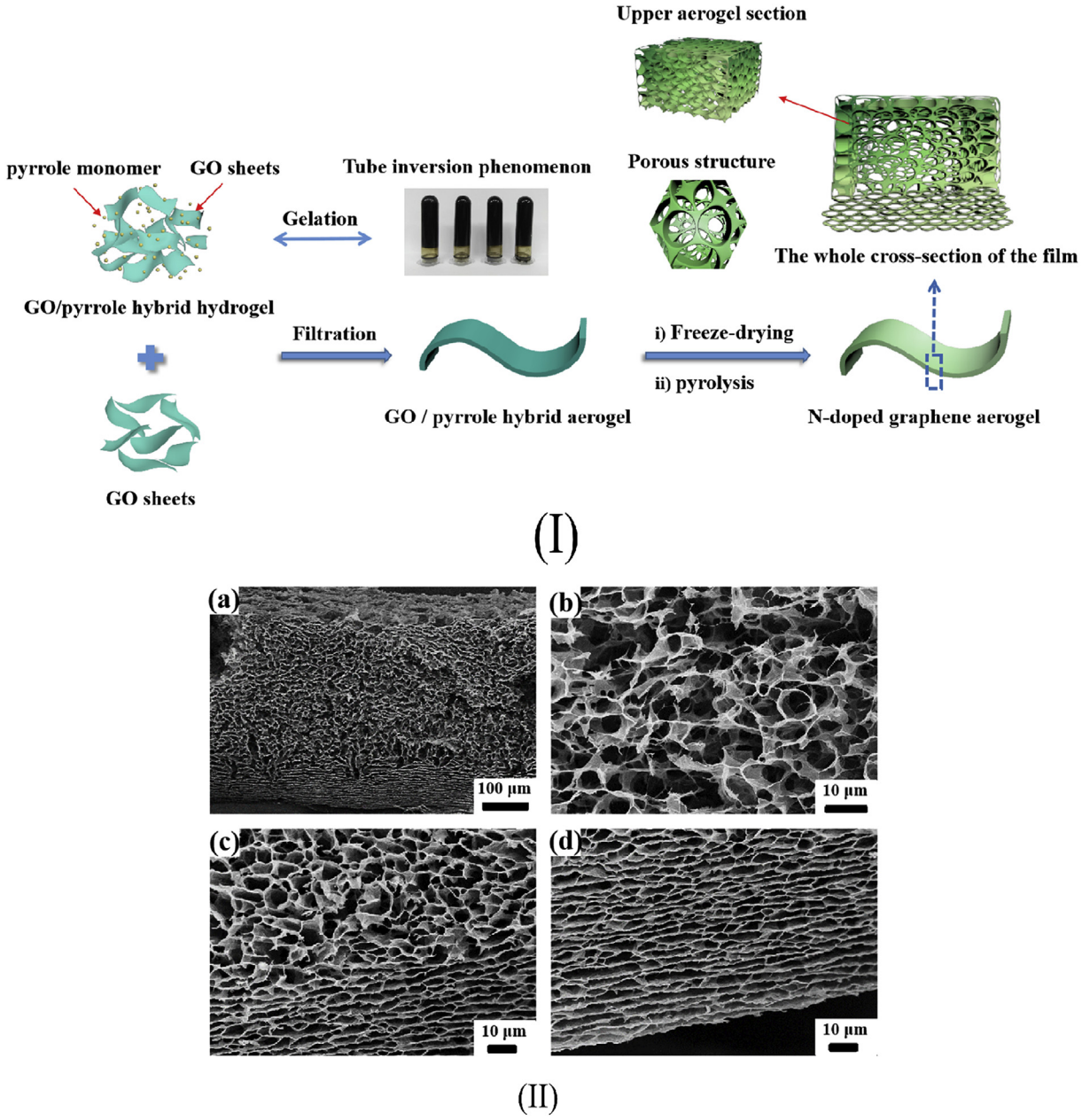

Fig. 1. (I) Schematic illustration of the fabrication process of N-doped graphene aerogel films. (II) (a–d) SEM images of different parts in the cross-section of the NG-3 film: (a) the whole cross-section; (b) the upper aerogel section; (c) the middle section; and (d) the bottom GO sheets section, respectively.

interconnected 3D framework network (Fig. S5a). The upper aerogel section with abundant well-defined macro-pores can be observed in Fig. S5b. High-magnification SEM image reveals that the pore walls are thick, which may due to PPy coating on the surfaces of graphene sheets in RGO/PPy-0.05 composite film (Fig. S5c).

XRD analysis shows that the diffraction peaks of GO appear at 11.1°, indicating the lamellar spacing is 0.77 nm (Fig. 2a). After pyrolysis, for NG-0, the peaks at 26.2 and 41.5° (representing (002) and (100) crystal planes) are observed [36]. While for NG-3 sample, there is an inconspicuous broad peak centered at about 25.5°, indicating the poor crystallinity of NG-3 sample. This further demonstrates the reduced aggregation of graphene sheets. Meanwhile, as shown in Figs. S5d and a similar broad peak appeared at ~23° is found in the patterns of PPy and RGO/PPy-0.05 composite film samples, indicating the amorphous structural feature. The weight ratio of PPy in RGO/PPy-0.05 sample was 48.78% (Fig. S7) calculated by TGA curve.

Raman spectra for GO and NG-x film (x = 0, 1, 2, 3 and 4) are recorded in Fig. 2b. Among these carbon materials, two peaks locating at 1300-1400 cm^{-1} and 1500-1600 cm^{-1} respectively are observed. These are attributed to the D band and G band of graphene [37–40]. The I_D/I_G values of NG-x (x = 0, 1, 2, 3, 4) samples are higher than that of pristine GO, and the value increases with the increase of the amount of Py monomer. This illustrates more defects were created [41]. Furthermore, the amount of defects increases along with the increase of Py, the nitrogen source. This suggests an influence of nitrogen doping. In FT-IR spectrum (Fig. S4), GO displays characteristic peaks at 3440, 1731, 1240 and 1168 cm^{-1}, corresponding to -OH, C=O, C-OH and C-O-C functional

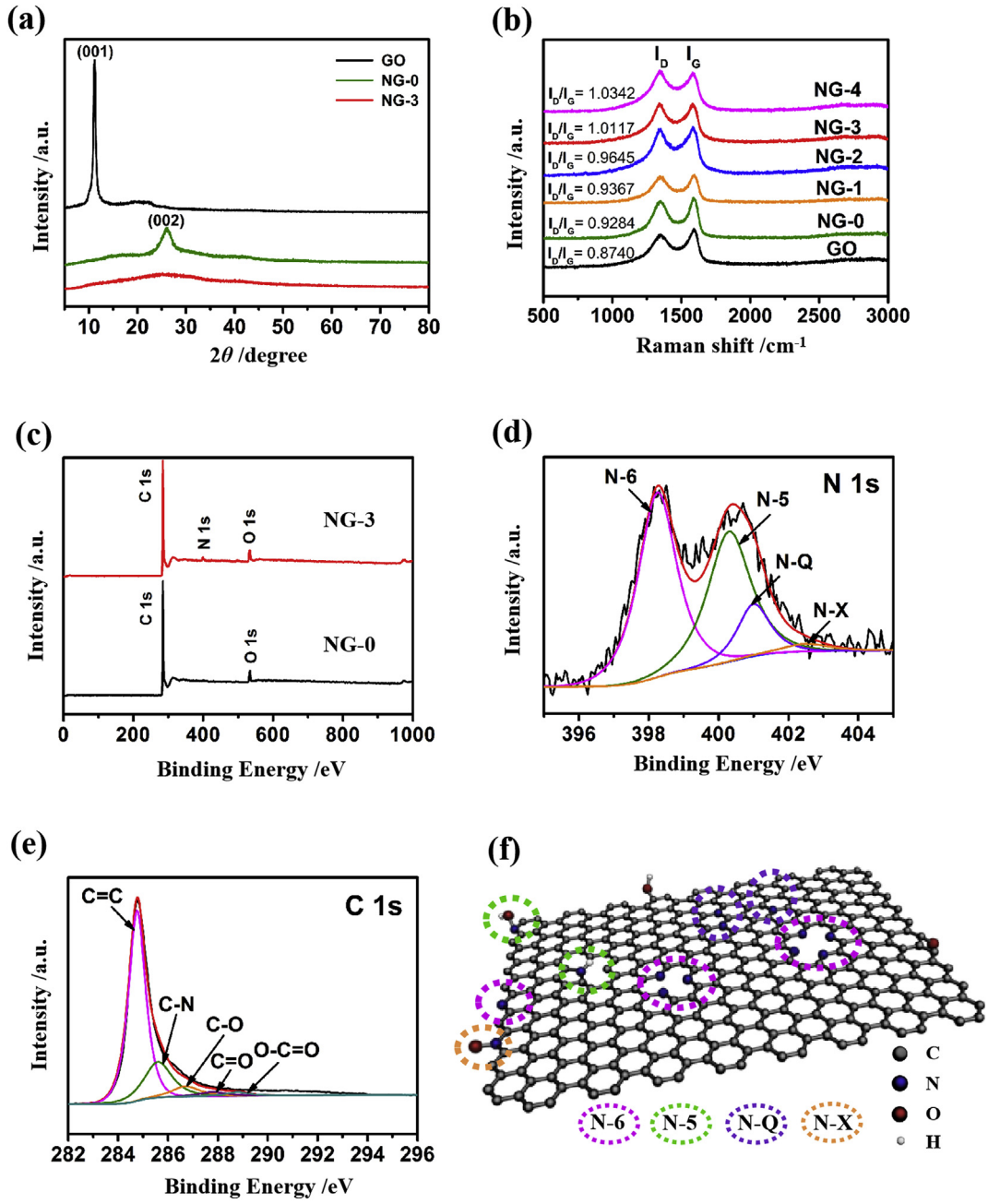

Fig. 2. (a) XRD patterns of GO, NG-0 film, NG-3 film. (b) Raman spectra of GO, NG-x films. (c) XPS survey spectrum for the NG-0 and NG-3 films. High-resolution XPS spectra of (d) N1s peak and (e) C1s peak of NG-3 film. (f) Schematic of nitrogen doping structure.

group stretching vibrations. NG-3 sample shows typical peaks at the range of 3300–3500, 1431 and 1173 cm^{-1}, which belongs to N-H, =C-N of pyrrole ring and C-N stretching vibrations, suggesting the incorporation of N atoms into carbon lattice. For the PPy powder sample, peaks ascribed to the N-H, C-N, =C-N, C-H vibrations and the skeleton vibration of the pyrrole rings can be observed at 3300-3500, 1431, 1218, 1048 and 1578 cm^{-1} respectively. RGO/PPy-0.05 composite shows the existence of almost all these peaks, confirming the successful synthesis of RGO/PPy composite.

The elemental species and nitrogen bonding configuration was further analyzed according to X-ray photoelectron spectroscopic (XPS) result. As displayed in Fig. 2c, all the samples exhibit signals of C1s peak at about 284.8 eV and O1s peak at 532.0 eV. Additionally, NG-3 films have a pronounced N1s peak at 400.0 eV, indicating the cooperation of nitrogen atom in carbon lattice. Moreover, the N content in NG-3 film is the highest among NG-x (x = 0, 1, 2, 3, 4) samples (Table S1). Meanwhile, the high resolution N1s peaks can be deconvoluted into four peaks (Fig. 2d), representing pyridinic N (N-6, 398.25 eV), pyrrolic/pyridone N (N-5, 400.30 eV), quaternary N (N-Q, 401.00 eV) and oxidized N (N-X, 402.50 eV), respectively [42]. Pyridine-N and pyrrole-N are the main N-bonding states in NG-3 film (Fig. S6, Table S2). As reported, pyridinic nitrogen and pyrrolic nitrogen are regarded as electrochemically active atoms, which are considered to be favorable to enhance the capacitance [43]. The spectrum of the C1s of NG-3 sample can be deconvoluted into five peaks at 284.6, 285.4, 286.9, 287.8 and 288.6 eV, attributed to the C=C, C–N, C–O, C=O

and O-C=O groups, respectively (Fig. 2e). Based on the Raman, FT-IR and XPS results, it is evident that nitrogen atoms have successfully incorporated in the carbon lattice. A schematic illustration of this structural arrangement is shown in Fig. 2f.

3.2. Electrochemical performance

The electrochemical properties of NG-x films (x = 0, 1, 2, 3 and 4) including cyclic voltammetry (CV), galvanostatic charge-discharge (GCD), electrochemical impedance spectroscopy (EIS) and cycling test were evaluated in a symmetrical two-electrode configuration using 0.5 M H_2SO_4 solution as the electrolyte (Fig. 3). Fig. 3a shows the CV curves of NG-x (x = 0, 1, 2, 3, 4) samples at the same scan rate of 10 mV s^{-1} with a potential window from 0 to 1 V. All CV curves show near rectangular shapes with symmetrical feature, illustrating a good capacitive behavior. The integrated area of CV curve of NG-3 is largest, implying the highest specific capacitance [44]. As plotted in Fig. 3b, discharge curves of all the N-doped graphene samples are nearly symmetrical triangle, suggesting nearly ideal reversible charge-discharge processes. For GCD curves, the area of the triangles implies the value of specific capacitance, which shows the similar trend as CV results. Obviously, the NG-3 film sample has the highest specific capacitance among all the samples. No obvious voltage drops at the initial stage of the discharge process are observed, indicating low internal series resistance (lower IR drop) [45].

The specific capacitance of the obtained electrode materials at current densities varying from 1 to 10 A g^{-1} are shown in Fig. 3c. All the samples show decreased specific capacitances as the current density increases. Among these samples, the NG-3 film shows the highest specific capacitance. Its highest gravimetric specific capacitance reaches 455.4 F g^{-1} at the current density of 1 A g^{-1}.

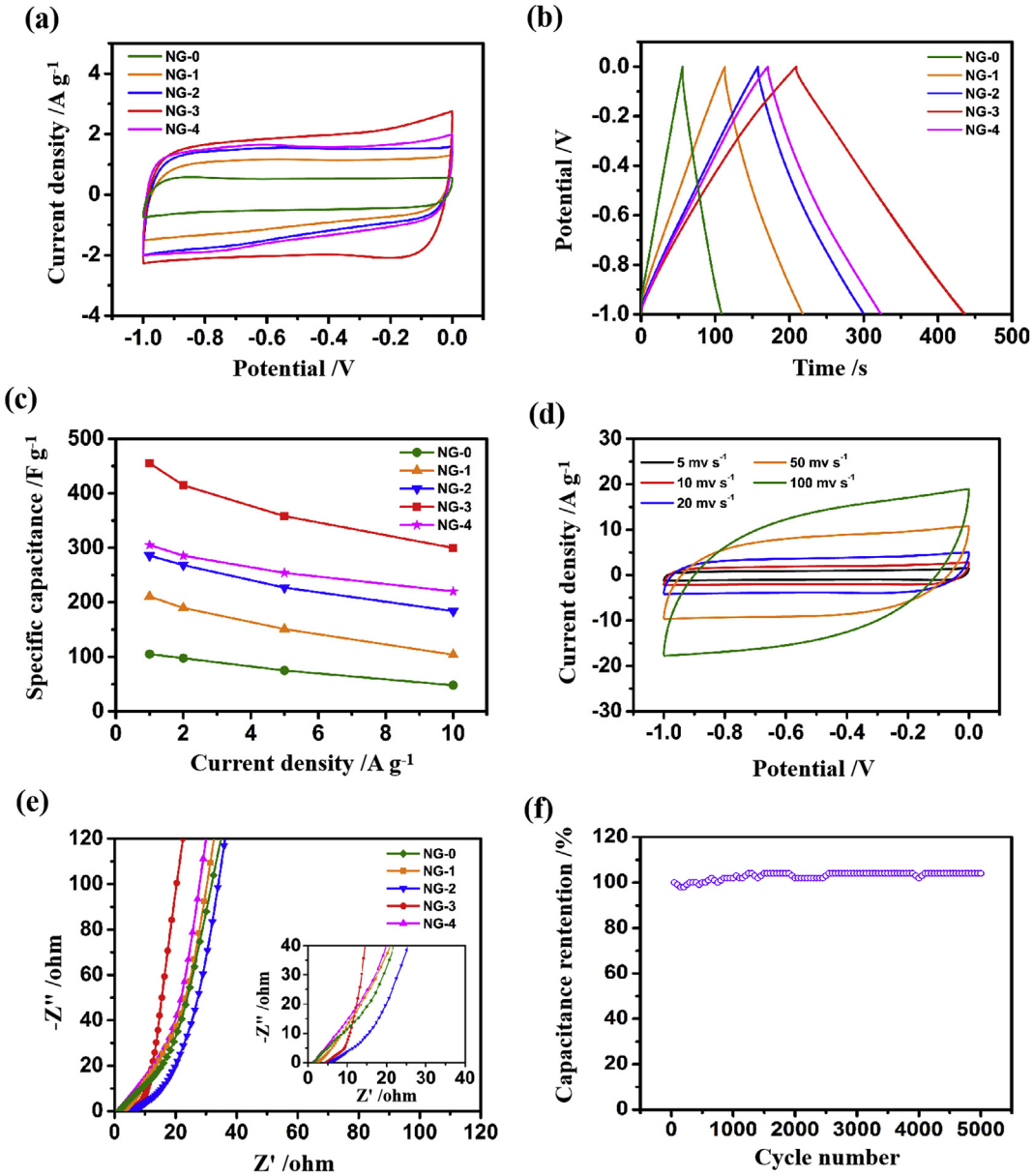

Fig. 3. Electrochemical performances of the NG-x (x = 1, 2, 3, 4) film electrodes: (a) CV curves at a scan rate of 10 mV s^{-1}; (b) Galvanostatic charge-discharge curves at a current density of 1 A g^{-1}; (c) Specific capacitance at various current densities; (d) CV curves of NG-3 film at various scan rates; (e) Nyquist plots; (f) Cyclic stability of NG-3 film at a current density of 5 A g^{-1}.

While for NG-0, NG-1, NG-2 and NG-4, the specific capacitance at the same current density is 105.2, 210.6, 285.8 and 305.2 F g^{-1}, respectively (Fig. 3c). Even at a high current density of 10 A g^{-1}, the specific capacitance of NG-3 film electrode still reaches 300.0 F g^{-1} exhibiting 66% retention ratio. The specific capacitance is higher than those of previously reported nitrogen-doped carbons, such as hNCNCs and N-CNFs-900 (Table 1). Rate performance is higher than those of nitrogen-doped hierarchical porous carbon materials (62% when varied to 10 A g^{-1}) [46], three-dimensional nitrogen-doped hierarchical porous carbon (42% when varied to 10 A g^{-1}) [47], and hierarchically porous N-doped carbon nanosheets (40% when varied to 10 A g^{-1}) [48]. What's more, the CV curves of the NG-3 film electrode collected at scan rates ranging from 5 to 100 mV s^{-1} all display rectangular profile, also indicating high rate performance (Fig. 3d). The outstanding rate performance of NG-3 film electrode could be caused by the synergistic effect between the highest N content and interconnected porous framework [49].

Nyquist plots are used to evaluate the resistance performance as displayed in Fig. 3e. They can reflect the charging and ion transfer properties in these electrode films. A well fitted equivalent circuit model of the EIS was plotted in Fig. S8. All of the samples show similar shape, consisting of a part of semicircle at high-frequency region and a near-vertical line in the low-frequency region. The two parts correspond to the combination of electrolyte resistance (Rs) and charge-transfer resistance (Rct), and the Warburg impedance representing the diffusive behaviors of the electrolyte in electrode pores and ions in active materials. In the high frequency region, the inconspicuous semicircles suggest low intrinsic resistance of the materials and fast faradaic charge transfer process [50]. At low-frequency, the NG-3 film shows a steeper slope than the other samples in the low frequency region, suggesting a higher ion mobility and diffusion of NG-3 electrode [51]. Besides, the cycling stability of NG-3 film was examined under a large current density of 5 A g^{-1} (Fig. 3f). The electrodes kept 104% of its initial capacitance after 5000 cycles. The slight increase may be caused by a slow activation process. No capacitance loss of the cycling performance demonstrates the good cyclic stability of the NG-3 film electrode. All of the measurement results mentioned above show the obvious advantage of electrochemical performance of the NG-x (x = 0, 1, 2, 3, 4) film electrodes. The excellent performance is caused by plentiful nitrogen active sites and better contact between electrolyte and electrode, contributed by abundant accessible surface area and pathways for ion transportation.

To fabricate an asymmetric SC device and obtain high energy density, we further fabricated RGO/PPy composite films with the similar structure. The electrochemical performance obtained in a two-electrode system is exhibited in Fig. S9. From CV curves of RGO/PPy-y (y = 0, 0.01, 0.05 and 0.1) samples in Fig. S9a, the enclosed area of CV curve for RGO/PPy-0.05 is the largest among the four samples, indicating the highest specific capacitance. Moreover, the CV profiles at variable scan rates (up to 100 mV s^{-1}) display quasi-rectangular shapes, suggesting its high rate capability. According to the GCD curves (Fig. S9b), the specific capacitance is calculated to be 460, 543.6, 740 and 670 F g^{-1} at the current density of 1 A g^{-1} for RGO/PPy-0, RGO/PPy-0.01, RGO/PPy-0.05 and RGO/PPy-0.1 respectively. The EIS analysis was conducted to evaluate the charge transfer and electrolyte diffusion behaviors, as recorded in Fig. S9d. The steeper shape of the sloped line represents an ideal capacitive behavior with the faster diffusion of ions in electrolyte. The RGO/PPy-0.05 electrode maintains 94.7% of the initial capacitance after 5000 cycles (Fig. S9f). The good electrochemical behavior can be ascribed to the good combination of the two materials and the interconnected pore structure of the electrode.

To achieve high energy density, an ASC device was assembled using RGO/PPy-0.05 composite film as the positive electrode and NG-3 film as the negative electrode (illustrated in Fig. S10a) denoted as RGO/PPy-0.05//NG-3. To do this, the stable potential window of each electrode was determined separately at first, using a symmetrical two-electrode system in 0.5 M H_2SO_4 at 20 mV s^{-1}. CV curves in Fig. 4a and Figs. S10b–c show that the NG-3 and RGO/PPy-0.05 films can work steadily in −1~0 and 0–1 V, respectively. When it is for RGO/PPy-0.05//NG-3 ASC device (Fig. 4b), the CV curves achieve ideal rectangular shape when the operating potential window is extended from 1.0 V to 1.7 V, reflecting excellent capacitive behavior. This can be attributed to good matching and combination of the two macro-porous electrodes. In Fig. 4c, all the CV curves retain quasi-rectangular shapes without any obvious redox peaks, when the scan rates increase from 5 to 200 mV s^{-1}. This suggests good rate performance and good reversibility of the device. As plotted in Fig. S10d, the near linear and symmetric GCD curves with no obvious IR drops can be observed at different current densities, indicating fast current/voltage response [52]. Impedance data in Fig. S10e with nearly vertical line at low frequency and inconspicuous semicircle in the high frequency region suggests high conductivity and rapid ion diffusion in the electrode [53].

According to equation (1), the specific capacitances for the ASC device are calculated based on the total mass of the electrodes, which are 86, 80.6, 70, 62.9 and 51.8 F g^{-1} at current densities of 1, 2, 5, 10 and 20 A g^{-1} respectively (Fig. 4d). That is, capacitance retention of 60.2% is observed. Further, the energy and power densities are calculated according to the galvanostatic discharge curves (based on equations (5) and (6)) and displayed in the Ragone

Table 1
Comparison of capacitive performances of this work with those reported in relevant works.

Electrode material	Specific capacitance	Device	Device capacitance	E_s@P_s	Electr-olyte	Operating voltage	Ref.
hNCNCs	313 F g^{-1}, 1 A g^{-1}	symmetric SC	313 F g^{-1}, 1 A g^{-1}	10.9 Wh kg^{-1} @250 W kg^{-1}	6.0 M KOH	0–1.0 V	[17]
N-CNFs-900	202 F g^{-1}, 1.0 A g^{-1}	symmetric SC	202 F g^{-1}, 1 A g^{-1}	5.38 Wh kg^{-1} @15000 W kg^{-1}	6.0 M KOH	0–1.0 V	[49]
GO_{10}/PPy composite	439 F g^{-1}, 5 mV s^{-1}	GO_{10}/PPy//AC	67.5 F g^{-1}, 0.6 A g^{-1}	21.4 Wh kg^{-1} @453.9 W kg^{-1}	1.0 M Na_2SO_4	0–1.6 V	[52]
N-CNTs	288 F g^{-1}, 1 mA cm^{-1}	PPy-NTs//N-CNTs	109 F g^{-1}, 1.43 A g^{-1}	28.98 Wh kg^{-1} @998.56 W kg^{-1}	1.0 M H_2SO_4	0–1.4 V	[54]
PPy@MnO_3 composite	110 F g^{-1}, 0.1 A g^{-1}	PPy@MnO_3//AC	58 F g^{-1}, 0.5 A g^{-1}	12 Wh kg^{-1} @3000 W kg^{-1}	0.5 M K_2SO_4	0–1.5 V	[55]
PPy/SnO_2 core/shell nanotube array	260 F g^{-1}, 1 A g^{-1}	PPy//MnO_2	67.8 F g^{-1}, 1 A g^{-1}	27.2 Wh kg^{-1} @850 W kg^{-1}	1.0 M Na_2SO_4	0–1.7 V	[56]
NG-3 film	**455.4 F g^{-1}, 1 A g^{-1}**	**RGO/PPy-0.05//NG-3**	**86 F g^{-1}, 1 A g^{-1}**	**34.5 Wh kg^{-1} @849.8 W kg^{-1}**	0.5 M H_2SO_4	**0–1.7 V**	**This work**

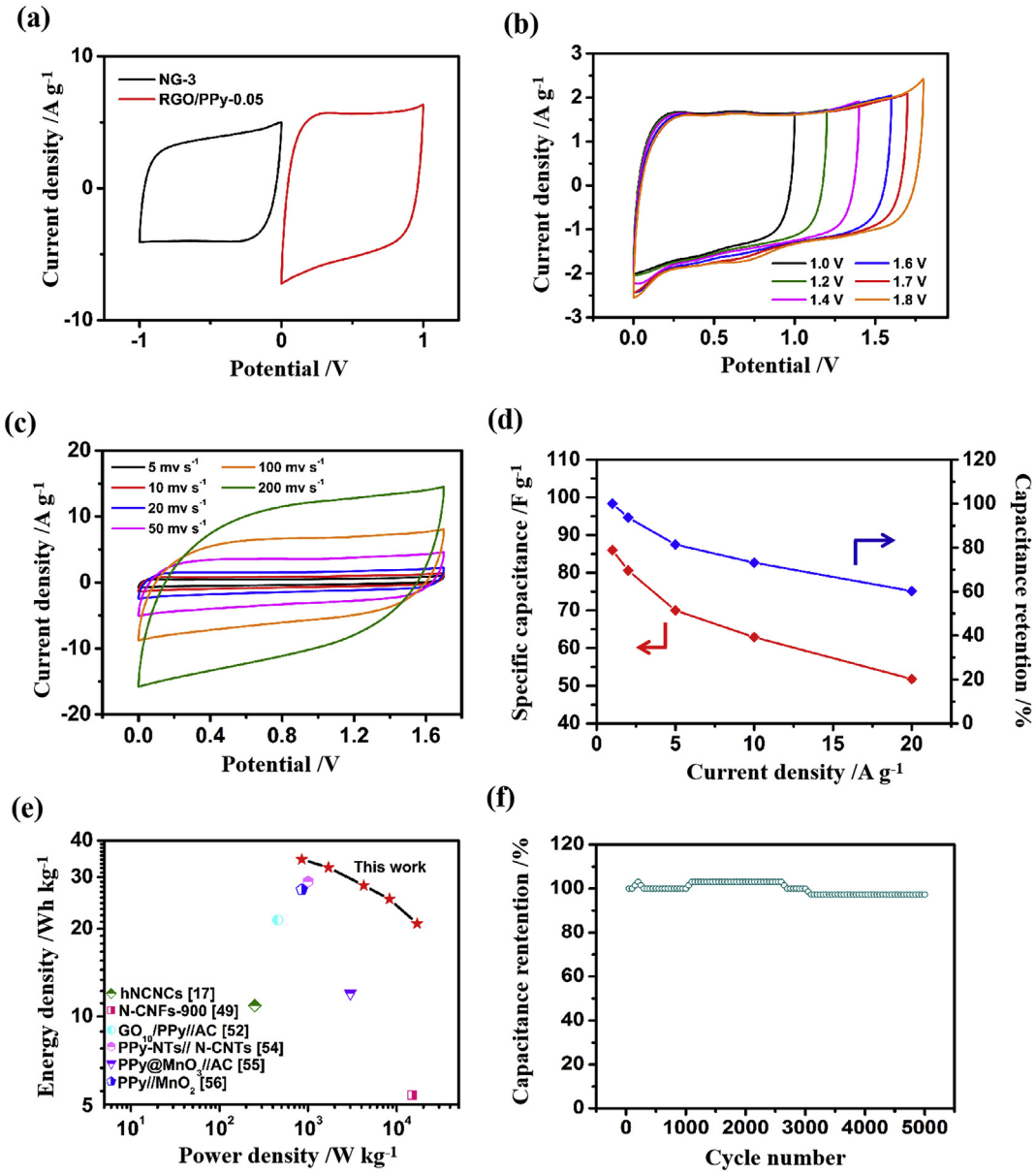

Fig. 4. (a) CV curves of NG-3 film and RGO/PPy-0.05 composite film at a scan rate of 20 mV s^{-1} and (b–f) electrochemical performance of the asymmetric supercapacitor RGO/PPy-0.05//NG-3: (b) CV curves at various potential windows at scan rate of 20 mV s^{-1}; (c) Nyquist plots for the asymmetric cell; (d) Specific capacitance and the corresponding capacitance retention at different current densities; (e) Ragone plots; (f) Cyclic stability at a current density of 5 A g^{-1}.

diagram (Fig. 4e). The assembled ASC device shows a maximum energy density of 34.5 Wh kg^{-1} at the power density of 849.8 W kg^{-1}. When the power density increases to 17 kW kg^{-1}, the energy density becomes 20.8 Wh kg^{-1} with a retention of 60.3%. The result is better than those of other reported values (Fig. 4e), hNCNCs (hierarchical nitrogen-doped carbon nanocages) symmetric SC (10.9 Wh kg^{-1} at a power density of 250 W kg^{-1}) [17], N-CNFs-900 symmetric SC (5.38 Wh kg^{-1} at a power density of 15 kW kg^{-1}) [49], GO_{10}/PPy//Activated carbon asymmetric SC (21.4 Wh kg^{-1} at a power density of 453.9 W kg^{-1}) [52], PPy-NTs (polypyrrole nanotubes)//N-CNTs (N-doped carbon nanotubes) asymmetric SC (28.98 Wh kg^{-1} at a power density of 998.56 W kg^{-1}) [54], PPy@MnO_3//Activated carbon asymmetric SC (12 Wh kg^{-1} at a power density of 3000 W kg^{-1}) [55], and PPy//MnO_2 asymmetric SC (27.2 Wh kg^{-1} at a power density of 850 W kg^{-1}) [56]. Furthermore, the assembled ASC device demonstrates excellent cycling stability with 97.4% of capacitance retention over 5000 cycles at 5 A g^{-1} (Fig. 4f, Table 1), which is comparable to those of other ASC devices.

4. Conclusions

In summary, we fabricated a novel porous free-standing graphene aerogel film for high energy density supercapacitor. The flexible film is composed of an NG aerogel upper part and a thin layer of well-organized graphene sheets at the bottom. The key point to the flexible and free-standing film is that, the graphene sheets in the bottom layer are highly arranged forming aligned macropores. Thus, the two parts can connect with each other tightly, and enhance the mechanical properties of the film. Due to the unique interconnected porous architecture and the effect of N incorporation, the resulted NG-3 film exhibits a specific capacitance

of 455.4 F g^{-1} and good rate performance. After 5000 cycles, the capacitance shows no obvious loss. To further achieve high energy density and evaluate the practical performance of the film, an ASC device is assembled with NG-3 as negative electrode. A series of RGO/PPy-y (y = 0, 0.01, 0.05 and 0.1) composite films were obtained by a similar strategy to use as the positive electrode of the ASC device, which show a similar two-layer microporous structure. The ASC device operated under a potential range of 0–1.7 V reaches a high energy density of 34.51 Wh kg^{-1} at a power density of 849.77 W kg^{-1}. The good energy storage performances can be ascribed to the unique porous structure of both NG-3 film and RGO/PPy composite film electrode, facilitating redox reaction kinetics in interconnected macro-pores in both electrodes. This design opens up a new pathway to create storage devices with outstanding power density and energy density for energy-based application.

Notes

The authors declare no conflicts of interest.

Acknowledgements

The authors are grateful for the financial support from the National Natural Science Foundation of China (21603058, 21704014, and 51433001), the Fundamental Research Funds for the Central Universities (2232017D-06), China Postdoctoral Science Foundation (2016M601471), Shanghai Sailing Program (17YF1400200), Program of Shanghai Academic Research Leader (17XD1400100), and Science and Technology Commission of Shanghai Municipality (16520722100).

Appendix A. Supplementary data

Supplementary data to this article can be found online at https://doi.org/10.1016/j.electacta.2019.06.107.

References

[1] H. Gwon, H.S. Kim, K.U. Lee, D.H. Seo, Y.C. Park, Y.S. Lee, B.T. Ahn, K. Kang, Flexible energy storage devices based on graphene paper, Energy Environ. Sci. 4 (2011) 1277–1283.
[2] Q. Lu, J.G.G. Chen, J.Q. Xiao, Nanostructured electrodes for high-performance pseudocapacitors, Angew. Chem. Int. Ed. 52 (2013) 1882–1889.
[3] V. Strong, M.F. El-Kady, S. Dubin, R.B. Kaner, Laser Scribing of High-performance and flexible graphene-based electrochemical capacitors, Science 335 (2012) 1326–1330.
[4] Y.W. Zhu, S. Murali, K.J. Ganesh, M.D. Stoller, W.W. Cai, P.J. Ferreira, A. Pirkle, R.M. Wallace, K.A. Cychosz, M. Thommes, D. Su, R.S. Ruoff, E.A. Stach, Carbon-based supercapacitors produced by activation of graphene, Science 332 (2011) 1537–1541.
[5] L. Yu, B.Y. Guan, W. Xiao, X.W. Lou, Formation of yolk-shelled Ni–Co mixed oxide nanoprisms with enhanced electrochemical performance for hybrid supercapacitors and lithium ion batteries, Adv. Energy Mater. 5 (2015) 1500981.
[6] Y.P. Zhai, Y.Q. Dou, D.Y. Zhao, P.F. Fulvio, R.T. Mayes, S. Dai, Carbon materials for chemical capacitive energy storage, Adv. Mater. 23 (2011) 4828–4850.
[7] A. Varzi, C. Schutter, J. Krummacher, R. Raccichini, C. Wolff, G.T. Kim, S. Rosler, B. Blumenroder, T. Schubert, S. Passerini, A. Balducci, A 4 farad high energy electrochemical double layer capacitor prototype operating at 3.2 V (IES prototype), J. Power Sources 326 (2016) 162–169.
[8] M.R. Lukatskaya, B. Dunn, Y. Gogotsi, Multidimensional materials and device architectures for future hybrid energy storage, Nat. Commun. 7 (2016) 12647.
[9] A.S. Arico, P. Bruce, B. Scrosati, J.M. Tarascon, W.V. Schalkwijk, Nanostructured materials for advanced energy conversion and storage devices, Nat. Mater. 4 (2005) 366–377.
[10] J. Chmiola, G. Yushin, Y. Gogotsi, C. Portet, P.L. Taberna, Anomalous increase in carbon capacitance at pore sizes less than 1 nanometer, Science 313 (2006) 1760–1763.
[11] T. Lv, Y. Yao, N. Li, T. Chen, Highly stretchable supercapacitors based on aligned carbon nanotube/molybdenum disulfide composites, Angew. Chem. Int. Ed. 55 (2016) 9191–9195.
[12] J.X. Zhu, L.J. Cao, Y.S. Wu, Y.J. Gong, Z. Liu, H.E. Hoster, Y.H. Zhang, S.T. Zhang, S.B. Yang, Q.Y. Yan, P.M. Ajayan, R. Vajtai, Building 3D structures of vanadium pentoxide nanosheets and application as electrodes in supercapacitors, Nano Lett. 13 (2013) 5408–5413.
[13] Y.H. Lee, Y.F. Lee, K.H. Chang, C.C. Hu, Synthesis of N-doped carbon nanosheets from collagen for electrochemical energy storage/conversion systems, Electrochem. Commun. 13 (2011) 50–53.
[14] J.Q. Yang, X.L. Zhou, D.H. Wu, X.D. Zhao, Z. Zhou, S-doped N-rich carbon nanosheets with expanded interlayer distance as anode materials for sodium-ion batteries, Adv. Mater. 29 (2017) 1604108.
[15] D. Hulicova-Jurcakova, M. Kodama, S. Shiraishi, H. Hatori, Z.H. Zhu, G.Q. Lu, Nitrogen-enriched nonporous carbon electrodes with extraordinary supercapacitance, Adv. Funct. Mater. 19 (2009) 1800–1809.
[16] T.Q. Lin, I.W. Chen, F.X. Liu, C.Y. Yang, H. Bi, F.F. Xu, F.Q. Huang, Nitrogen-doped mesoporous carbon of extraordinary capacitance for electrochemical energy storage, Science 350 (2015) 1508–1513.
[17] J. Zhao, H.W. Lai, Z.Y. Lyu, Y.F. Jiang, K. Xie, X.Z. Wang, Q. Wu, L.J. Yang, Z. Jin, Y.W. Ma, J. Liu, Z. Hu, Hydrophilic hierarchical nitrogen-doped carbon nanocages for ultrahigh supercapacitive performance, Adv. Mater. 27 (2015) 3541–3545.
[18] K.X. Zou, Y.F. Deng, J.P. Chen, Y.Q. Qian, Y.W. Yang, Y.W. Li, G.H. Chen, Hierarchically porous nitrogen-doped carbon derived from the activation of agriculture waste by potassium hydroxide and urea for high-performance supercapacitors, J. Power Sources 378 (2018) 579–588.
[19] X.J. He, P.H. Ling, J.S. Qiu, M.X. Yu, X.Y. Zhang, C. Yu, M.D. Zheng, Efficient preparation of biomass-based mesoporous carbons for supercapacitors with both high energy density and high power density, J. Power Sources 240 (2013) 109–113.
[20] T.Y. Kim, G.J. Jung, S.M. Yoo, K.S. Suh, R.S. Ruoff, Activated graphene-based carbons as supercapacitor electrodes with macro- and mesopores, ACS Nano 7 (2013) 6899–6905.
[21] M. Zhou, F. Pu, Z. Wang, S.Y. Guan, Nitrogen-doped porous carbons through KOH activation with superior performance in supercapacitors, Carbon 68 (2014) 185–194.
[22] A. Varzi, R. Raccichini, M. Marinaro, M. Wohlfahrt-Mehrens, Stefano Passerini, Probing the characteristics of casein as green binder for non-aqueous electrochemical double layer capacitors' electrodes, J. Power Sources 326 (2016) 672–679.
[23] Y. Hu, H.H. Cheng, F. Zhao, N. Chen, L. Jiang, Z.H. Feng, L.T. Qu, All-in-one graphene fiber supercapacitor, Nanoscale 6 (2014) 6448–6451.
[24] A. Khosrozadeh, M.A. Darabi, M. Xing, Q. Wang, Flexible electrode design: fabrication of freestanding polyaniline-based composite films for high-performance supercapacitors, ACS Appl. Mater. Interfaces 8 (2016) 11379–11389.
[25] J.Y. Tang, P. Yuan, C.L. Cai, Y.B. Fu, X.H. Ma, Combining nature-inspired, graphene-wrapped flexible electrodes with nanocomposite polymer electrolyte for asymmetric capacitive energy storage, Adv. Energy Mater. 6 (2016) 1600813.
[26] M.S. Zhu, Y. Huang, Q.H. Deng, J. Zhou, Z.X. Pei, Q. Xue, Y. Huang, Z.F. Wang, H.F. Li, Q. Huang, C.Y. Zhi, Highly flexible, freestanding supercapacitor electrode with enhanced performance obtained by hybridizing polypyrrole chains with MXene, Adv. Energy Mater. 6 (2016) 1600969.
[27] H.M. Jeong, J.W. Lee, W.H. Shin, Y.J. Choi, H.J. Shin, J.K. Kang, J.W. Choi, Nitrogen-doped graphene for high-performance ultracapacitors and the importance of nitrogen-doped sites at basal planes, Nano Lett. 11 (2011) 2472–2477.
[28] L.F. Chen, Z.H. Huang, H.W. Liang, W.T. Yao, Z.Y. Yu, S.H. Yu, Flexible all-solid-state high-power supercapacitor fabricated with nitrogen-doped carbon nanofiber electrode material derived from bacterial cellulose, Energy Environ. Sci. 6 (2013) 3331–3338.
[29] J.Z. Chen, J.L. Xu, S. Zhou, N. Zhao, C.P. Wong, Nitrogen-doped hierarchically porous carbon foam: a free-standing electrode and mechanical support for high-performance supercapacitors, Nano Energy 25 (2016) 193–202.
[30] Y. Song, T.Y. Liu, X.X. Xu, D.Y. Feng, Y. Li, X.X. Liu, Pushing the cycling stability limit of polypyrrole for supercapacitors, Adv. Funct. Mater. 25 (2015) 4626–4632.
[31] D.G. Jiang, H. Liang, W.R. Yang, Y. Liu, X.Y. Cao, J.M. Zhang, C.W. Li, J.Q. Liu, J.J. Gooding, Screen-printable films of graphene/CoS_2/Ni_3S_4 composites for flexible and arbitrary-shaped all-solid-state hybrid supercapacitor device, Carbon 146 (2019) 557–567.
[32] G.P. Wang, L. Zhang, J.J. Zhang, A review of electrode materials for electrochemical supercapacitors, Chem. Soc. Rev. 41 (2012) 797–828.
[33] M. Yang, Z. Zhou, Recent breakthroughs in supercapacitors boosted by nitrogen-rich porous carbon materials, Adv. Sci. 4 (2017) 1600408.
[34] W.S. Hummers, R.E. Offeman, Preparation of graphitic oxide, J. Am. Chem. Soc. 80 (1958), 1339-1339.
[35] W. Deng, Q.L. Fang, H.R. Huang, X.F. Zhou, J.B. Ma, Z.P. Liu, Oriented arrangement: the origin of versatility for porous graphene materials, Small 13 (2017) 1701231.
[36] D.C. Zhang, X. Zhang, Y. Chen, P. Yu, C.H. Wang, Y.W. Ma, Enhanced capacitance and rate capability of graphene/polypyrrole composite as electrode material for supercapacitors, J. Power Sources 196 (2011) 5990–5996.
[37] G.H. Yu, X. Xie, L.J. Pan, Z.N. Bao, Y. Cui, Hybrid nanostructured materials for high-performance electrochemical capacitors, Nano Energy 2 (2013) 213–234.
[38] L.L. Liu, Z.Q. Niu, L. Zhang, W.Y. Zhou, X.D. Chen, S.S. Xie, Nanostructured graphene composite papers for highly flexible and foldable supercapacitors,

Adv. Mater. 26 (2014) 4855–4862.
[39] A.L.M. Reddy, A. Srivastava, S.R. Gowda, H. Gullapalli, M. Dubey, P.M. Ajayan, Synthesis of nitrogen-doped graphene films for lithium battery application, ACS Nano 4 (2010) 6337–6342.
[40] G.M. Wang, H.Y. Wang, X.H. Lu, Y.C. Ling, M.H. Yu, T. Zhai, Y.X. Tong, Y. Li, Solid-State supercapacitor based on activated carbon cloths exhibits excellent rate capability, Adv. Mater. 26 (2014) 2676–2682.
[41] D.S. Geng, Y. Chen, Y.G. Chen, Y.L. Li, R.Y. Li, X.L. Sun, S.Y. Ye, S. Knights, High oxygen-reduction activity and durability of nitrogen-doped graphene, Energy Environ. Sci. 4 (2011) 760–764.
[42] Z.H. Sheng, L. Shao, J.J. Chen, W.J. Bao, F.B. Wang, X.H. Xia, Catalyst-free synthesis of nitrogen-doped graphene via thermal annealing graphite oxide with melamine and its excellent electrocatalysis, ACS Nano 5 (2011) 4350–4358.
[43] M. Yang, Y.R. Zhong, J. Bao, X.L. Zhou, J.P. Wei, Z. Zhou, Achieving battery-level energy density by constructing aqueous carbonaceous supercapacitors with hierarchical porous N-rich carbon materials, J. Mater. Chem. A 3 (2015) 11387–11394.
[44] C.G. Liu, Z.N. Yu, D. Neff, A. Zhamu, B.Z. Jang, Graphene-based supercapacitor with an ultrahigh energy density, Nano Lett. 10 (2010) 4863–4868.
[45] W.J. Qian, F.X. Sun, Y.H. Xu, L.H. Qiu, C.H. Liu, S.D. Wang, F. Yan, Human hair-derived carbon flakes for electrochemical supercapacitors, Energy Environ. Sci. 7 (2014) 379–386.
[46] J. Zhou, Z.S. Zhang, W. Xing, J. Yu, G.X. Han, W.J. Si, Nitrogen-doped hierarchical porous carbon materials prepared from meta-aminophenol formaldehyde resin for supercapacitor with high rate performance, Electrochim. Acta 153 (2015) 68–75.
[47] Y.Y. Yin, R.Y. Li, Z.J. Li, J.K. Liu, Z.G. Gu, G.L. Wang, A facile self-template strategy to fabricate three-dimensional nitrogen-doped hierarchical porous carbon/graphene for conductive agent-free supercapacitors with excellent electrochemical performance, Electrochim. Acta 125 (2014) 330–337.
[48] Y.Y. Wang, B.H. Hou, H.Y. Lu, C.L. Lu, X.L. Wu, Hierarchically porous N-doped carbon nanosheets derived from grapefruit peels for high-performance supercapacitors, ChemistrySelect 1 (2016) 1441–1446.
[49] L.F. Chen, X.D. Zhang, H.W. Liang, M.G. Kong, Q.F. Guan, P. Chen, Z.Y. Wu, S.H. Yu, Synthesis of nitrogen-doped porous carbon nanofibers as an efficient electrode material for supercapacitors, ACS Nano 6 (2012) 7092–7102.
[50] Y.L. Cheng, L. Huang, X. Xiao, B. Yao, L.Y. Yuan, T.Q. Li, Z.M. Hu, B. Wang, J. Wan, J. Zhou, Flexible and cross-linked N-doped carbon nanofiber network for high performance freestanding supercapacitor electrode, Nano Energy 15 (2015) 66–74.
[51] H.L. Wang, Q.L. Hao, X.J. Yang, L.D. Lu, X. Wang, Effect of graphene oxide on the properties of its composite with polyaniline, ACS Appl. Mater. Interfaces 2 (2010) 821–828.
[52] L.Q. Fan, G.J. Liu, J.H. Wu, L. Liu, J.M. Lin, Y.L. Wei, Asymmetric supercapacitor based on graphene oxide/polypyrrole composite and activated carbon electrodes, Electrochim. Acta 137 (2014) 26–33.
[53] Y.L. Shao, M.F. El-Kady, C.W. Lin, G.Z. Zhu, K.L. Marsh, J.Y. Hwang, Q.H. Zhang, Y.G. Li, H.Z. Wang, R.B. Kaner, 3D freeze-casting of cellular graphene films for ultrahigh power-density supercapacitors, Adv. Mater. 28 (2016) 6719–6726.
[54] D.P. Dubal, N.R. Chodankar, Z. Caban-Huertas, F. Wolfart, M. Vidotti, R. Holze, C.D. Lokhande, P. Gomez-Romero, Synthetic approach from polypyrrole nanotubes to nitrogen doped pyrolyzed carbon nanotubes for asymmetric supercapacitors, J. Power Sources 308 (2016) 158–165.
[55] Y. Liu, B.H. Zhang, Y.Q. Yang, Z. Chang, Z.B. Wen, Y.P. Wu, Polypyrrole-coated a-MoO_3 nanobelts with good electrochemical performance as anode materials for aqueous supercapacitors, J. Mater. Chem. A 1 (2013) 13582–13587.
[56] F. Grote, Y. Lei, A complete three-dimensionally nanostructured asymmetric supercapacitor with high operating voltage window based on PPy and MnO_2, Nano Energy 10 (2014) 63–70.